

On the large-scale radiative cooling induced by tropical cyclone activity

Gabriel A. Rios^{a,b,1}, Gabriel A. Vecchi^{b,c,2}, and Wenchang Yang^{b,c,3}

This manuscript was compiled on July 13, 2025

Tropical cyclones (TCs) are among the most energetic phenomena in the climate system.

tropical cyclones | tropical climate | convective aggregation | climate change

The climate system is regulated by the tropical energy budget. The tropics receive a positive net annual radiative flux, which is balanced by poleward energy transport (1, 2). Given the importance of clouds in modulating energy in the climate system, it follows that understanding the radiative properties of tropical clouds is critical. In the tropics, deep convection is an important mechanism for regulating the energy balance, through the condensational heating of the atmosphere and by modifying the radiative heating of the tropics. In addition to the radiative properties of deep convective clouds, studies have shown that the organization of deep convection is also important for modulating tropical climate, with studies indicating that convective aggregation increases radiative cooling by drying of the free troposphere (3–8). Moreover, there is evidence that the degree of tropical convective aggregation may change with a warming climate, although it is unclear in what direction and to what extent this may occur (3, 9–11).

A ubiquitous type of organized deep convection is the tropical cyclone (TC). TCs generally originate in the tropics and aggregate moisture and cloud cover into long-lived coherent structures that can travel thousands of kilometers. For this reason, TCs are also considered as intense, albeit localized, examples of convective aggregation (12–15). TCs have also been shown to advect energy both vertically and meridionally, rendering TCs a unique form of deep convection. As with large-scale convective aggregation, it is anticipated that TC frequency and/or intensity will change with a warming climate, although a consensus on precisely how has not yet been reached, though peak intensity of the strongest TCs is expected to increase (16–18). Although TCs are small and infrequent relative to other deep convective phenomena, their energetic nature and ability to transport heat and moisture suggests they have upscale impacts on the climate system (19).

In this study, we use global climate models (GCMs) to show that TCs induce radiative cooling across different scales and timeframes. These results were obtained through a comparison of control and modified GCM configurations, which produce climate systems with realistic and suppressed TC activity, respectively. At storm-scale, TCs result in reduced net incoming top-of-atmosphere radiation by reflecting more incident solar radiation from high cloud tops than the longwave radiation trapped by deep cloud cover. In GCM runs with fixed sea-surface temperatures, TC activity is found to induce large-scale cooling due to increases longwave emission to space by aggregating column water vapor and cloud cover. When the ocean model is coupled to the atmospheric model, TC activity is found to increase radiative cooling due to heightened longwave emissions as a result of reduced atmospheric moisture content from cooled SSTs.

Known impacts of TCs on the climate system. A significant body of work exists investigating radiative properties of TCs and the effects of radiative feedbacks on TC evolution; we refer the reader to (20, 21) for more information. However, the radiative effects of TCs on the climate have not been widely analyzed; our study therefore focuses on this topic.

Several studies have provided insights on these effects through direct (e.g., modulation of radiative transfer at top of atmosphere, column radiative heating) and indirect mechanisms (e.g., reduction of sea-surface temperatures, localized humidity changes). Using observational techniques, the indirect radiative effects of TC have primarily been

Significance Statement

Although the effects of the large-scale climate on tropical cyclones (TCs) are well-known, it is unclear how TC properties will evolve in a changing climate. In this work, we approximate the upscale effect of TCs on the climate system to understand their feedback on the large-scale environment using observational data and global climate model simulations. We show that TCs act to radiatively cool the climate system on various spatiotemporal scales. Evidence is also presented for the role of TCs in organizing tropical convection through modifications to sea-surface temperature patterns. This work aims to add to a body of research quantifying the impacts of TCs on the climate system to help reduce uncertainty in projections of future climates.

Author affiliations: ^aProgram in Atmospheric and Oceanic Sciences, Princeton University, Princeton, NJ 08540; ^bDepartment of Geosciences, Princeton University, Princeton, NJ 08540; ^cHigh Meadows Environmental Institute, Princeton, NJ 08540

G.A.R., G.A.V., and W.Y. designed research; G.A.R., G.A.V., and W.Y. performed research; G.A.R., G.A.V., and W.Y. contributed new reagents/analytic tools; G.A.R. analyzed data; G.A.R. wrote the paper.

The authors declare no competing interests.

²To whom correspondence should be addressed. E-mail: gr7610@princeton.edu

attributed to reductions in sea-surface temperature (SST) generated by cold wakes following the passage of TCs (22–25). (22) used a composite analysis to establish correlations between TC-induced cold wakes and reductions in local precipitation and cloud coverage. Although not explicitly discussed in the study, the correlations have implications for the radiative budget, given that decreased cloud cover increases the amount of solar radiation leaving the surface and the amount of longwave radiation emitted to space. The relevance of these implications is addressed in (24), in which the importance of obtaining a radiative budget associated with TC passage is stressed due to its relevance to tropical radiation in TC-active basins. (25) builds upon the studies of (24) by providing a novel composite analysis of radiative impacts associated with TCs, finding that despite having a small net radiative effect during TC passage, the cold wakes generated by TCs can result in radiative cooling anomalies reaching 1 W m^{-2} relative to the observational climatology.

Analyses using idealized numerical models have also posited that indirect radiative effects associated with TCs are a result of convective aggregation. Several studies simulating rotating convection in a periodic domain have noted the positive correlation between TC intensity and domain-averaged longwave cooling (12, 14, 26) due to an aggregation of deep convection (which manifests as a TC when Earth's rotation is considered) in a small portion of the domain, resulting in an increase in domain fraction constituted of dry air that is largely transparent to radiation.

The work on indirect radiative effects of TCs has shown that an investigation of direct TC radiative properties is critical for fully understanding the role of TCs on the radiative budget. (27) performed one of the first such analyses by cataloguing composite radiative properties of TCs from observational data to investigate the role of radiative heating in TC intensification. A notable result from this study is the correlation between cloud radiative effect intensity and TC intensity. As expected, the cloud radiative effect increases with TC intensity. However, the cloud radiative effect for the area surrounding the TC featured a negative correlation with TC intensity, as negative feedbacks became stronger with increasing TC intensity. This aligns with a similar analysis performed in (21) using a global climate modeling approach to investigate the role of radiative feedbacks on TC development. As noted in these studies, this trend shows consistency with findings from idealized studies of TCs and has implications on the role of TCs in convective aggregation.

Recently, observational approaches to investigating direct radiative effects of TCs have been pursued. To the authors' knowledge, (28) is the first study that estimates the global radiative effect of TCs on the climate system, finding that TC activity contributes to net radiative cooling of 26 TW yr^{-1} . The analysis used 1° CERES observational data to estimate the radiative contributions of TCs, ultimately finding that radiative cooling is driven by the increase in reflected solar radiation at TOA.

The results from the aforementioned studies provide evidence of the radiative impacts of TCs on the climate system beyond any given storm. This analysis attempts to build on these findings by employing observational data and long-run global climate model (GCM) simulations. These studies are performed in an effort to understand the radiative

impacts of TCs on the climate system by connecting the radiative effects of TCs across spatial and temporal scales.

The first portion of this study focuses on radiative effects at the TC-scale, which will also be referred to as "small-scale" due to the spatial extent of the analysis. This portion of the study begins by investigating the radiative characteristics of TCs using a composite analysis of observational and GCM data to catalogue radiative properties of TCs. The study extends the compositing approach to investigate the direct radiative effects of TCs on the mean climate state using TC anomalies from the climatology. Note that the term "direct effect" refers to anomalies occurring at the location of TC occurrence, whereas the term "indirect effect" will refer to anomalies occurring away from TCs.

The second portion of this study expands in scope to investigate the radiative effects associated with TC activity at the climate scale, which will interchangeably be referred to as "large-scale". This portion of the analysis is performed using a comparison of results from GCM experiments with realistic and suppressed TC activity to reveal differences in the Earth's energy budget associated with TC activity. These experiments are performed in GCMs with fixed-SST (AMIP-style) and coupled atmosphere-ocean (CMIP-style) to analyze the ocean feedback to radiative effects associated with TC activity.

Results

Case study: climatological anomalies associated with a mature TC. To begin understanding the upscale effects of TCs on the climate, a case study of a single simulated TC is analyzed. The TC studied occurs in CM2.5-FLOR (coupled atmosphere-ocean GCM) over the western Pacific Ocean during the late summer, with genesis occurring due east of the Philippines (roughly 141° E , 18° N), followed by an approach to continental Asia while a reaching lifetime maximum intensity at approximately 950 hPa, and eventually beginning a poleward recurvature; following a track typical of TCs in the Western Pacific. Figure 1 provides snapshots of anomalies from the model climatology during TC passage on select days between genesis and lysis.

Expectedly, anomalies of column water vapor (Figure 1a-d) reveal a strong moist anomaly at the TC location (maximum value of $+28.8 \text{ kg m}^{-2}$) and a weaker dry anomaly (minimum value of -12.3 kg m^{-2}) surrounding the TC as it travels through the basin; this spatial pattern demonstrates the role of a TC as a local aggregator of moisture. Sea-surface temperature (SST) anomalies (Figure 1e-h) reveal a negative anomaly exceeding 3 K trailing the TC, reminiscent of cold wakes that are commonly observed following TC passage (23, 29, 30). Anomalies from the climatology of TOA net radiation (R_{TOA} , Figure 1i-l) show decreased R_{TOA} at the location of the TC and increased R_{TOA} over the area surrounding the TC. Anomalies of R_{TOA} were largest at the TC center at peak intensity (TC day 6), reaching diurnally-averaged values of -200 W m^{-2} , with the surrounding domain exhibiting positive anomalies below $+100 \text{ W m}^{-2}$ albeit over a larger area than the negative anomalies. This pattern indicates that the direct radiative effects of the TC are local cooling and nonlocal heating relative to the climatology.

The evolution of anomaly spatial patterns and magnitudes over the lifetime of the TC indicates a correlation between

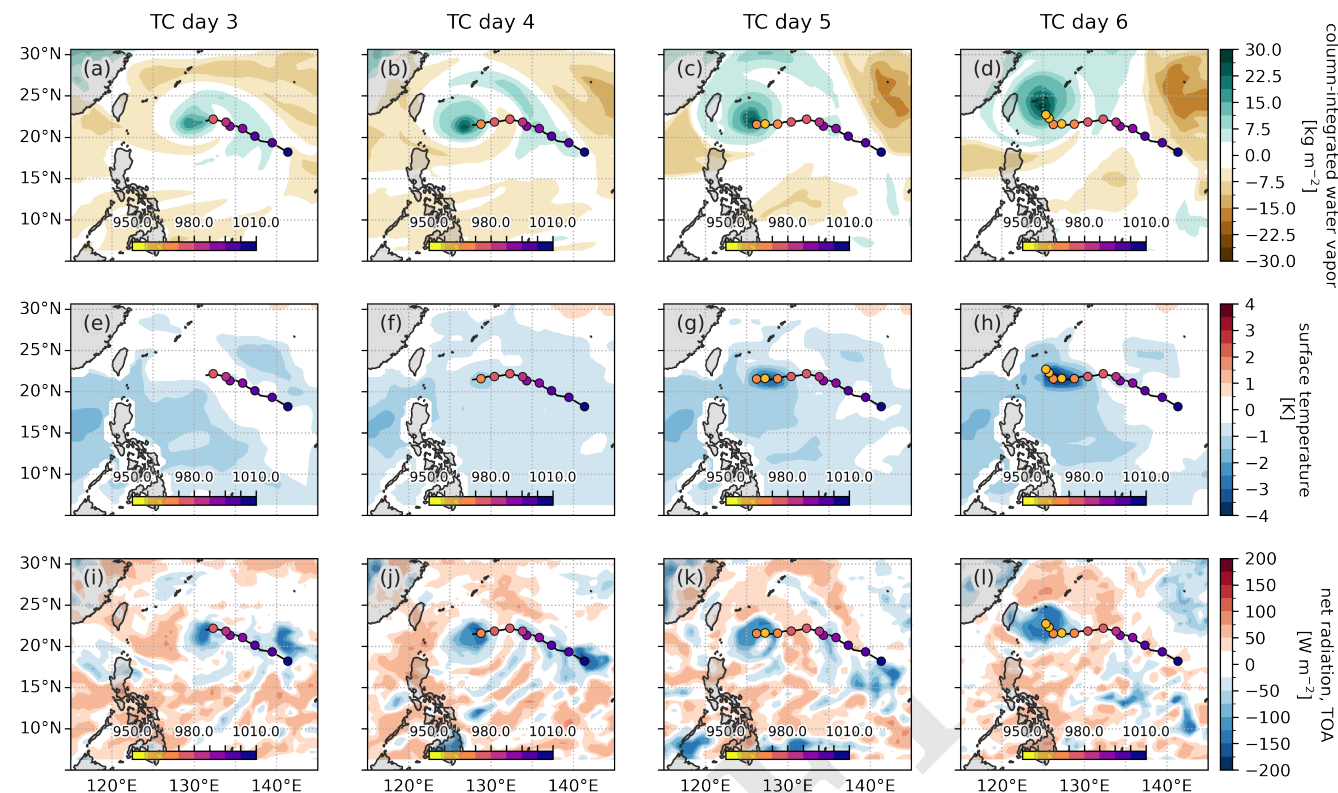


Fig. 1. Snapshots from CM2.5-FLOR of anomalies from the model climatology during the passage of a mature simulated TC over the western Pacific Ocean. Climatological anomalies shown are column-integrated water vapor (top row, panels a-d), and sea-surface temperature (SST, center row, panels e-h), and top-of-atmosphere net radiation (R_{TOA} , bottom row, panels i-l). The climatology is generated from daily means of a 100-year CM2.5-FLOR model integration, filtered using a 5-day rolling average. The anomaly is generated as the difference during a TC day from the climatology. The dotted line shows the TC track, with colors corresponding to minimum sea-level pressure (in units of hPa) as denoted by the horizontal colorbar.

TC intensity and anomaly strength. The difference in column water vapor anomalies between the TC and its surroundings increases as the TC intensifies, providing clear evidence of the TC as a localized aggregator of moisture relative to the mean climate state. The SST anomaly also demonstrated evidence of a relationship with TC intensity given the increased cooling effect with increased TC intensity. However, the SST anomaly also demonstrated a correlation with TC translation speed; SST cooling intensified with slower TC translation speed (29). The localized aggregation of column water vapor and sea-surface cooling induced by the TC contributed to the anomalies of R_{TOA} at the TC and its surroundings. An increase in TC column moisture is associated with anomalously-deep convection and higher cloud tops, resulting in net radiative cooling. Given the localized aggregation, a reduction in moisture and cloud cover surrounding the TC results in increased opacity to radiation, producing a radiative heating anomaly relative to the mean climate state. This is aided by the decrease in emitted longwave radiation associated with reduced SSTs, albeit to a small degree.

Composite analysis of TC radiative properties. Building on the patterns exhibited by a case study of a single TC, we generalize the direct radiative effects of TCs using composite analysis of TC snapshots.

Composite analysis of TC-centered top-of-atmosphere net incoming radiation (R_{TOA}) (see Fig. 2a-i) shows domains with composite mean minima of R_{TOA} at the TC center and increasing R_{TOA} with distance from the TC center. Observations of TCs derived from CERES show composite mean minima (which correspond to TC centers) ranging between 20 and 30 $W m^{-2}$ (in agreement with findings in (31)) with outer domain R_{TOA} values increasing to the range from 80 to 100 $W m^{-2}$. Data derived from TCs in GCMs show similar spatial patterns to those from observations, albeit with lower R_{TOA} values at TCs, with AM2.5 featuring composite mean minima ranging between -8 and -10 $W m^{-2}$ and CM2.5-FLOR minima ranging between -20 and -30 $W m^{-2}$. Observational data show weaker cooling anomalies than GCM data; a decomposition into ASR and OLR reveals that the discrepancy between observational and GCM data is dominated by ASR. This is found to be at least partially a function of spatial resolution; upwards shortwave radiation increases with cloud top height, representation of high cloud tops in TCs improves with increasing spatial resolution, and the GCMs used have higher spatial resolutions than the observational dataset.

To quantify the impacts of TCs on the R_{TOA} climatology, composite anomalies of TCs from the climatology (R'_{TOA}) were derived. Composite mean R'_{TOA} reveal the TOA radiative cooling effect of TCs relative to the mean climate state. Peak radiative anomaly magnitudes range across datasets

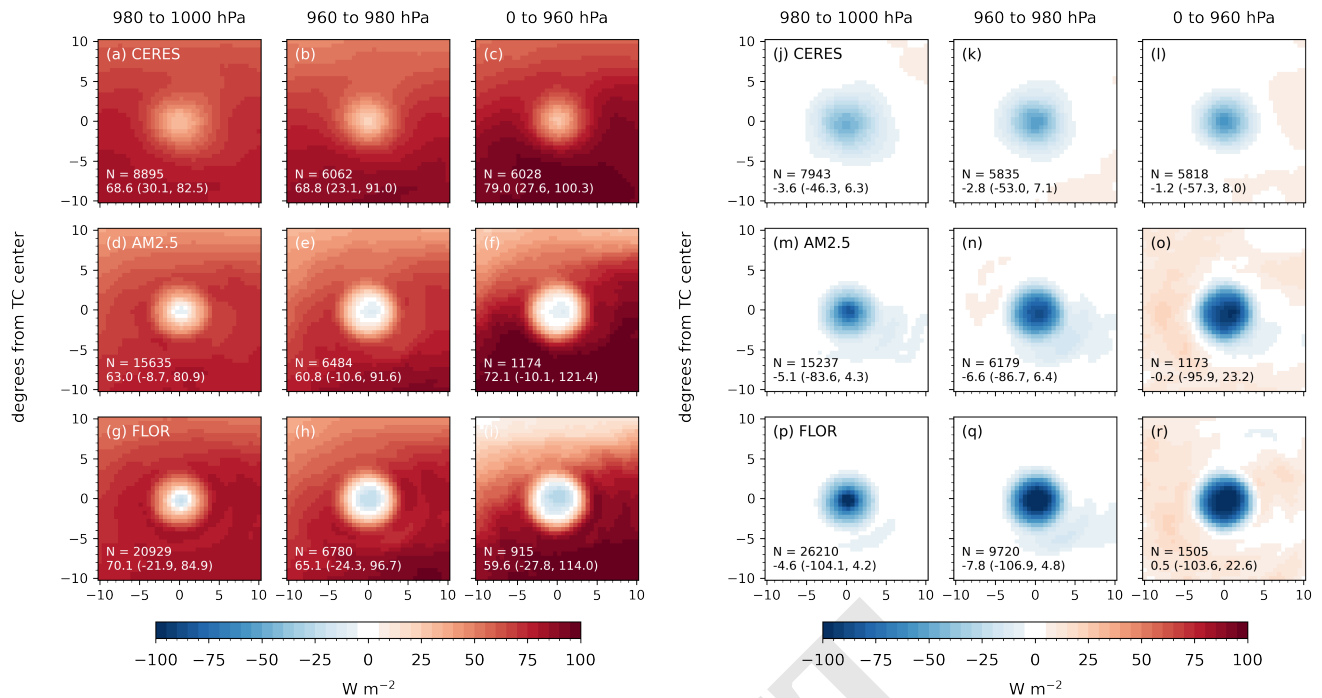


Fig. 2. TC-centered composite mean values of R_{TOA} (panels a-i) and composite mean climatological anomalies of R_{TOA} (panels j-r) for TCs in CERES (top row, panels a-c and j-l), AM2.5 (center row, panels d-f and m-o), and CM2.5-FLOR (bottom row, panels g-i and p-r). TC composites are divided by intensity into weak TCs (minimum sea-level pressure greater than or equal to 980 hPa), moderate-intensity TCs (960 to 980 hPa), and strong TCs (less than 960 hPa).

from -50 to -100 W m^{-2} for weak TCs (maximum intensity of 980 to 1000 hPa) and -60 to -120 W m^{-2} for strong TCs (below 960 hPa). The radiative cooling is driven by an increase in reflected shortwave radiation at TOA that exceeds the increase in trapped outgoing longwave radiation. Composite-mean radiative properties also exhibit a correlation with TC intensity; radiative anomalies (corresponding to a radiative cooling anomaly) decrease with increasing TC intensity at the TC core, while radiative anomalies (radiative heating anomaly) increase with increasing TC intensity outside the TC core.

Climate-scale impacts of TC activity.

Top-of atmosphere net radiation. The difference in annually-averaged R_{TOA} between control and SWISHE model runs is analyzed for AM2.5 (Figure 3a) and CM2.5-FLOR (Figure 3b).

In the fixed-SST runs, AM2.5 exhibits a reduction in R_{TOA} over large swaths of the subtropics with increased TC activity. Reductions in R_{TOA} exceeding 2 W m^{-2} occur over the northwestern Pacific, the northern Indian, and the southwestern Indian Oceans. Virtually all basins with TC activity experience a reduction in R_{TOA} , although the extent of net radiative cooling also extends throughout the entire subtropical Pacific and into the midlatitudes. The only region with a robust warming signal is the eastern tropical Pacific, featuring annually-averaged increases in R_{TOA} exceeding 2 W m^{-2} with more TC activity. In areas with TC activity exceeding a threshold of 0.5 TC days per year, the difference in R_{TOA} is neutral to strongly negative, particularly in the subtropical western Pacific. The zonal mean of annually-averaged differences in R_{TOA} roughly

reflects these patterns; a zonally-averaged increase in R_{TOA} at the equator of approximately 0.4 W m^{-2} is flanked by decreases in R_{TOA} in the subtropics and midlatitudes. This pattern also exhibits a hemispheric asymmetry, with more pronounced radiative cooling in the Northern Hemisphere than the Southern Hemisphere. Moreover, the peak zonally-averaged decrease in R_{TOA} occurs between 15 and 20 degrees N, which is the latitude featuring the strongest zonally-averaged reduction in TC activity. Decomposing zonal-mean R_{TOA} into shortwave and longwave components reveals a strong zonal-mean increase in absorbed shortwave (ASR) radiation at the equator, partially offset by an increase in outgoing longwave radiation (OLR). The longwave response becomes dominant away from the equator, with zonal-mean increases in OLR mirroring changes in TC activity.

When the ocean is allowed to couple to the atmosphere in CM2.5-FLOR, the R_{TOA} response to an increase in TC activity exhibits a notably different spatial pattern than the response in AM2.5 with fixed SSTs. Similar to AM2.5, reductions in R_{TOA} reach local maxima over the northwestern Pacific Ocean of approximately 2 W m^{-2} , although reductions of similar magnitude occur in the east and central Pacific as well as the southwestern Pacific. Additionally, reductions of R_{TOA} in CM2.5-FLOR in the Indian Ocean occur equatorward of similar reductions in AM2.5. The tropical Pacific demonstrates a dipole pattern of R_{TOA} in response to TC activity; with increased TC activity, the western tropical Pacific exhibits a net radiative warming while the eastern tropical Pacific exhibits a net cooling. Outside of the tropical Pacific, swaths of the subtropical and northern Pacific exhibited increases in R_{TOA} with increased TC activity. The zonal mean annually-averaged difference of R_{TOA} exhibits a

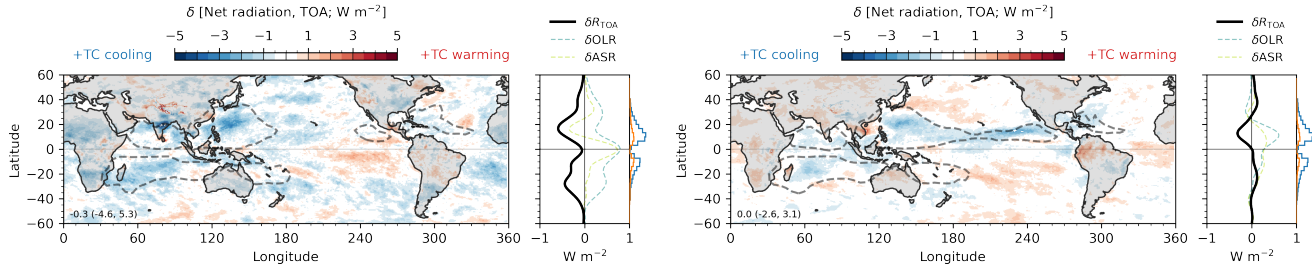


Fig. 3. Annual-mean TOA net radiation (R_{TOA}) difference (denoted by the delta operator, δ) between control and SWISHE experiments for AM2.5 (top row) and CM2.5-FLOR (bottom row) model integrations. Time mean differences are shown in the left column and zonal-time mean differences are shown in the right column. Zonal-time mean differences of R_{TOA} are decomposed into shortwave and longwave components. Blue and green histograms correspond to relative TC frequency as a function of latitude for the control and SWISHE experiments, respectively. The dashed contour denotes the extent of 0.5 TC days per year. Stippling denotes statistical significance at the 95% confidence interval using a bootstrapping method.

bimodal pattern of TOA radiative cooling associated with TC activity, with a small increase in zonal mean R_{TOA} at the equator flanked by decreases in zonal mean R_{TOA} of roughly 0.5 W m^{-2} . As in AM2.5, the peak values of the zonal mean differences in R_{TOA} occur at similar latitudes to those featuring the strongest zonally-averaged reduction in TC activity. The decomposition of the zonal-mean R_{TOA} response in CM2.5-FLOR reveals that the meridional pattern of the zonal-mean radiative response is driven by changes to OLR. A notable difference from AM2.5 is the suppressed equatorial increase of ASR despite a similar increase in zonal-mean R_{TOA} ; this is attributed to a corresponding decrease in tropical longwave emissions with TC activity.

A key distinction in the R_{TOA} response to TC activity between the fixed-SST and coupled GCM is the role of outgoing longwave radiation in determining R_{TOA} . When SST is held constant, reductions in ASR are offset by reductions in OLR in many places, resulting in small changes to R_{TOA} . This results in a R_{TOA} response to TC activity that, despite correlating with the spatial extent of TC activity, features a relatively weak spatial coherence. In contrast, the R_{TOA} response in the coupled GCM is much more spatially-coherent and correlated with the spatial extent of TC activity. The R_{TOA} response to TC activity primarily occurs in the tropics and subtropics and is roughly coterminous with the spatial extent of TC activity (with the exception of a weak warming signal in the north Pacific, see Figure 3b). This provides evidence for the role the ocean plays in determining the radiative response of the climate system to TC activity. If one considers the climate response in the fixed-SST simulation to represent feedbacks on a short timescale (i.e., ocean not given sufficient time to respond to forcing), the cancellation of shortwave and longwave radiation aligns with findings from (25).

High cloud fraction. TC activity is shown to negatively correlate with high cloud fraction in the tropics and subtropics (see 4). In both GCMs, cloud cover at 200 hPa decreases with TC activity at almost every location with TC activity. The exception is the Arabian Sea, which suggests that TCs provide a large portion of climatological high cloud cover in this basin.

In AM2.5, planar-time means shown in Figure 4a, the maximum reduction in 200 hPa cloud fraction occurs over the Maritime Continent, with reductions exceeding 2%. Reductions in 200 hPa cloud fraction extend throughout other TC basins, notably in the eastern Pacific and poleward

edges of TC activity in all TC-active regions. Interestingly, an increase in 200 hPa cloud fraction of approximately 2% occurs in the eastern Indian Ocean, creating a dipole pattern response in high cloud amount, resembling a weakening of the Indian Ocean branch of the Walker Circulation. As demonstrated by the zonal-time mean diagrams against pressure and latitude (see Figure 4b), the dominant cloud response to TC activity occurs in the upper troposphere, with peak reductions occurring at the equator (dominated by the aforementioned reduction in high cloud cover over the Maritime Continent) and the subtropics. Although the strongest reductions in cloud fraction occur in the upper troposphere, a statistically-significant zonal-mean reduction occurs throughout the tropospheric column at the equator, which shifts meridionally depending on the time of year in tandem with the seasonality TC activity (not shown).

When the ocean is coupled in CM2.5-FLOR, the distribution of high cloud response shifts poleward relative to AM2.5 to resemble the meridional pattern of TC activity. Maximum reductions in 200 hPa cloud fraction occur in the subtropical western Pacific and tropical southern Indian Ocean, coincident with areas of high TC activity in CM2.5-FLOR. Other areas with notable TC activity, such as the north Atlantic, northern Indian, and southwestern Pacific Oceans, present robust annual-mean reductions in 200 hPa cloud fraction generally exceeding 1%. Despite not being directly influenced by TC activity, the central-eastern tropical Pacific exhibits a swath of reduced 200 hPa cloud fraction reaching 1.5% extending from 190 to 270° E. This sets up a dipole with the western tropical Pacific, as the region coincident with the Pacific Warm Pool exhibits an increase in high cloud fraction reaching 2%. Similar to AM2.5, zonal mean diagrams against pressure and latitude show robust reductions to subtropical high cloud fraction as a function of TC activity, with lesser impacts throughout the remainder of the free troposphere.

TC-induced SST cooling. Over the 100 yr GCM model integrations provided, TC activity is shown to result in SST cooling (see Figure 5). To the authors' knowledge, the results obtained using long-term GCM integrations and the SWISHE algorithm demonstrate a correlation between TC activity and SST cooling within and outside of TC-active areas for the first time. Regarding long-term integrations of direct TC effects on SSTs, TC activity is shown to reduce SSTs throughout the majority of the subtropics and throughout portions of the midlatitudes in both hemispheres. In addition, increased

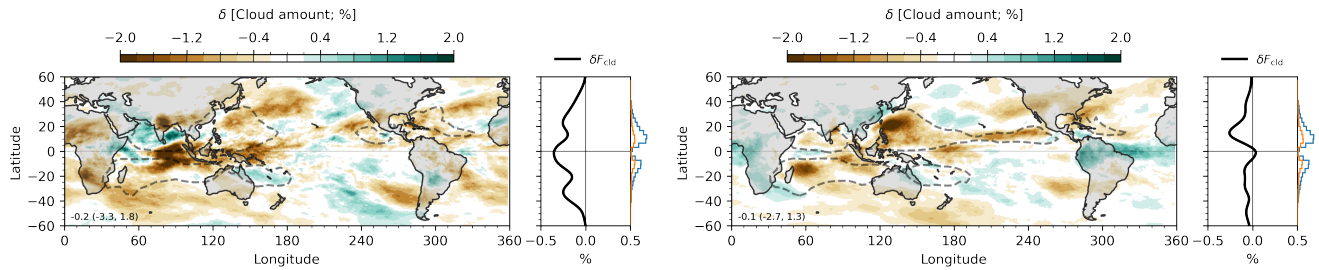


Fig. 4. Annual mean difference (denoted by the delta operator, δ) in cloud cover between control and SWISHE experiments for AM2.5 (top row, panels a-b) and CM2.5-FLOR (bottom row, panels c-d) model integrations. Planar-time mean differences are shown in the left column and time mean differences are shown in the right column. Blue and green histograms correspond to relative TC frequency as a function of latitude for the control and SWISHE experiments, respectively. Stippling denotes statistical significance at the 95% confidence interval using a bootstrapping method.

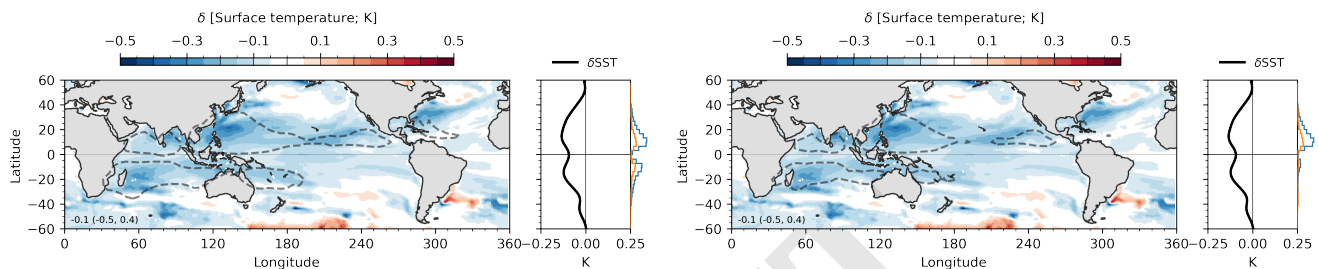


Fig. 5. Annual-mean (panel a) and July-December mean (panel b) sea-surface temperature (SST) differences (denoted by the delta operator, δ) between control and SWISHE experiments for CM2.5-FLOR model integrations. Planar-time mean differences are shown in the left column and zonal-time mean differences are shown in the right column of each panel. Blue and green histograms correspond to relative TC frequency as a function of latitude for the control and SWISHE experiments, respectively. The dashed contour denotes the extent of 0.5 TC days per year. Stippling denotes statistical significance at the 95% confidence interval using a bootstrapping method.

TC activity is correlated with SST reductions in the eastern tropical Pacific despite little to no cooling of the Pacific warm pool, suggesting modifications to the tropical Pacific thermocline tilt. Reductions to TC activity in CM2.5-FLOR are correlated with zonal and time-mean SST reductions of approximately 0.15 K over the 100 yr model integration, with maximum reductions occurring in areas with high TC activity. For example, the western North Pacific experiences annual-mean SST reductions of approximately 0.6 K, although this can exceed 0.8 K for boreal summer when TC activity is highest.

The spatial pattern and magnitude of SST cooling due to TC activity is evidently related to differences in radiative properties between control and SWISHE GCM integrations. As shown by the response of high cloud fraction in CM2.5-FLOR and . The impacts of TC activity on high cloud fraction are found to vary between AM2.5 and CM2.5-FLOR, further emphasizing the role of ocean feedbacks when considering the effects of TC activity on radiation.

Discussion.

Direct and indirect upscale effects of TCs on radiative cooling.

Results provide evidence that TC effects are scale-dependent in space and time. Considering direct effects on the TC-scale (i.e., small spatial scale and short time scale), composite analysis showed the role of TCs in inducing TOA radiative cooling where they occur. This is attributed to strong reductions to ASR that outweigh reductions to OLR, particularly relative to the mean climate state. Although beyond the scope of this discussion, we note that consideration of the diurnal variation of TOA radiative effects is important

when analyzing the direct radiative effects of TCs, as noted in other studies of TC radiative properties (28), and future work will investigate the dependence of TC radiative effects on the diurnal cycle.

The indirect effects of TC activity on the large-scale environment (i.e., large spatial scale) can be considered on both a short and a long timescale, where the timescale length is dictated by the response time of the upper ocean. Results from AM2.5 (i.e., fixed SSTs) can be considered the short-term climate response, as the upper ocean has not had the opportunity to respond to atmospheric forcing. The short-term response is characterized by net zonal-mean reductions in incoming radiation throughout the subtropics driven by increased OLR, with a modest increase in the tropics driven by an increase in ASR (see SI Appendix, Fig. 7). In several basins, despite similar reductions in R_{TOA} in the zonal-mean and the TC-scale, the radiative components of the zonal-mean response (increase in OLR outweighs decrease in ASR) differ from the direct TC response (decrease in OLR is outweighed by increase in ASR) (see Figure 3). Analysis shows that in TC-active areas, the direct TC radiative response dominates as shown by stronger increases in ASR than reductions in OLR, but areas without high TC activity demonstrate that reductions in column water vapor result in increased OLR. A notable exception is the R_{TOA} response to TC activity in the eastern Pacific Ocean, which features high TC activity but exhibits modest net cooling largely due to increased OLR and is likely explained by reductions in marine stratocumulus cloud cover which strongly reflect solar radiation (32).

Focusing on TC-active areas, this analysis demonstrates that modifications of high cloud fraction with TC activity

drives a net radiative cooling with TC activity. Figure 4a shows reductions in high cloud fractions in areas with TC activity, although the strongest reductions in high clouds occur over the eastern Indian Ocean and Maritime Continent. Evaluating the vertical structure of the cloud response indicates a robust, albeit small, decrease in cloud fraction throughout the atmospheric column to varying magnitudes, resulting in increases to OLR and even larger increases to ASR. Although the mechanism contributing to this is unclear, one hypothesis is the role of TCs serving as eddies that advect moist static energy poleward and weaken mean tropical ascent, although this requires further analysis.

In comparison, results from CM2.5-FLOR can be considered the long-term climate response given the coupling of the ocean to the atmosphere. The long-term climate response to TC activity is similarly characterized by reductions to incoming radiation throughout the tropics due to increases in OLR, although the spatial patterns are notably more constrained to the extent of TC activity as shown in Figures 3 and 4. Extending the previous discussion of the short-term climate response, the equatorial reduction in cloud fraction with TC activity evident in AM2.5 has vanished in CM2.5-FLOR despite a persistence of high cloud reductions in the subtropics throughout TC-active latitudes, suggesting an equilibration of the climate system in response to the tropical radiative anomalies over the eastern Indian Ocean and Maritime Continent. The equilibration is significantly influenced, if not driven by, the SST cooling pattern induced by TC activity. Considering indirect effects on the climate scale (i.e., large spatial scale and long time scale), TC activity induces a net cooling effect that is driven by increases to OLR. This increase in OLR is primarily attributable to the reduction in subtropical high cloud fraction.

The role of TC activity in convective aggregation. The results presented provide evidence of a positive correlation between TC activity and convective aggregation at both spatial scales evaluated.

At small spatial scales (i.e., storm-scale), TCs are shown to increase radiative cooling locally by decreasing ASR more than they reduce OLR through consolidation of moisture and deep clouds into a coherent structure, with upper-level outflow leading to expanse high cloud tops. This process results in a reduction of optical depth in the domain surrounding the TC due to decreases in high cloud fraction (Figure 4a-b) and column water vapor (SI Appendix, Figure 6) relative to climatology, which agree with results from studies of convective aggregation in idealized numerical models (14, 26, 33, 34). As expected, these effects appear to be a function of TC intensity as shown in composite anomalies in Figure 2 due to increases in cloud top heights and low-level convergence associated with strong TCs.

At larger scales (i.e., basin-scale), TC activity is correlated with reductions in high cloud fraction (Figure 4). The reductions in high cloud fraction have common and differing features between GCM runs with fixed SSTs and a coupled ocean. Results from both GCM configurations demonstrate annual-mean reductions in high cloud fraction where TC activity occurs. The decreases in high cloud fraction align with findings of idealized studies that find reductions in high cloud cover in a domain with convective storms (such as TCs) (12, 26, 34, 35) due to drying and increased subsidence

of the domain surrounding deep convection. However, the spatial distribution of reductions in high cloud fraction varies between GCMs; a reduction in the tropics is strongest in AM2.5, while a subtropical reduction is strongest in CM2.5-FLOR (see Figure 4, panels b and d). The disparity in responses is partially explained by the SST response as shown in Figure 4c: lower SSTs correspond to a drier troposphere and increased cooling, predominantly due to increased OLR, while such a pattern is not seen for AM2.5 (Figure 4a).

Materials and Methods

Global climate models. GCMs used in this analysis are an atmosphere-only GCM, AM2.5, and a coupled atmosphere-ocean GCM, CM2.5-FLOR. CM2.5-FLOR (Forecast Low-Ocean Resolution) (36) is a modification of the GFDL coupled atmosphere-ocean GCM, CM2.5 (37), that modulates ocean resolution as a function of latitude to increase computational efficiency, while maintaining high resolution ($\leq 1^\circ$) in the tropics and subtropics. The decreased ocean resolution is adequate for the purpose of this study, which is focused on atmospheric phenomena (i.e., TCs). Flux adjustment is implemented in CM2.5-FLOR runs to reduce biases of mean SST and surface wind stress in CM2.5 relative to observations, resulting in improved representations of the mean climate state and TC activity relative to CM2.5 (36). AM2.5 is the atmospheric component of GFDL coupled atmosphere-ocean GCM CM2.5, which is run with fixed sea-surface temperatures prescribed as a repeated monthly climatology computed from the United Kingdom's Met Office Hadley Centre Sea Ice and Sea Surface Temperature dataset (38) averaged from years 1986 to 2005.

AM2.5 and CM2.5-FLOR feature spatial resolutions of 0.5° in the atmosphere, while CM2.5-FLOR modulates ocean resolution from 1° at the poles to approximately 0.33° at the equator. Model integrations of 50 yr and 100 yr were obtained for AM2.5 and CM2.5-FLOR, respectively, for data analysis. CM2.5-FLOR was spun-up for 2000 yr prior to the model integration period used for analysis to allow for climate system equilibration.

CERES satellite-derived fluxes. Radiative fluxes are obtained using data from the NASA Clouds and Earth's Radiant Energy System (CERES) Synoptic dataset (CERES-SYN1deg-Ed4.1) (39). The spatial resolution of the dataset is 1° by 1° with a temporal resolution of 1 h. The dataset provides shortwave and longwave radiative fluxes at TOA, with post-observational adjustments performed using a radiative transfer model. CERES data from 2001 to 2020 are used for this study.

The global-mean bias of ASR in CM2.1 (from which CM2.5 is derived) relative to CERES-EBAF-Ed2.8 is -2.01 W m^{-2} (40), although biases generally range between -10 and $+10 \text{ W m}^{-2}$ in areas with TC activity exceeding 0.5 TC d yr^{-1} .

SWISHE algorithm for suppressing TC activity. The upscale effects of TCs on climate is estimated by comparing two climate states: one with realistic TC activity (control) and one with suppressed TC activity (experiment). To estimate the effect of TC activity on the climate system, the difference between control and the experiment climate systems is obtained. To generate a climate state with suppressed TC activity, the SWISHE algorithm is implemented on the GCMs used in this study (41). The SWISHE (i.e., suppressed WISHE) algorithm suppresses evaporation in model grid cells that satisfy criteria characteristic of TC activity. The algorithm reduces TC frequency significantly in the GCMs evaluated in this study; over the model years used for analysis herein, TC frequency is reduced by 59.7% and 63.8% over all intensities in AM2.5 and CM2.5-FLOR, respectively, with reductions of 93.8% and 92.8% for hurricane-strength TCs in AM2.5 and CM2.5-FLOR, respectively.

TC-centered composite analysis. TC anomalies from climatology are defined as $x' = x - \bar{x}$, where x' represents the anomaly, x is the observed quantity, and \bar{x} is the climatological time mean.

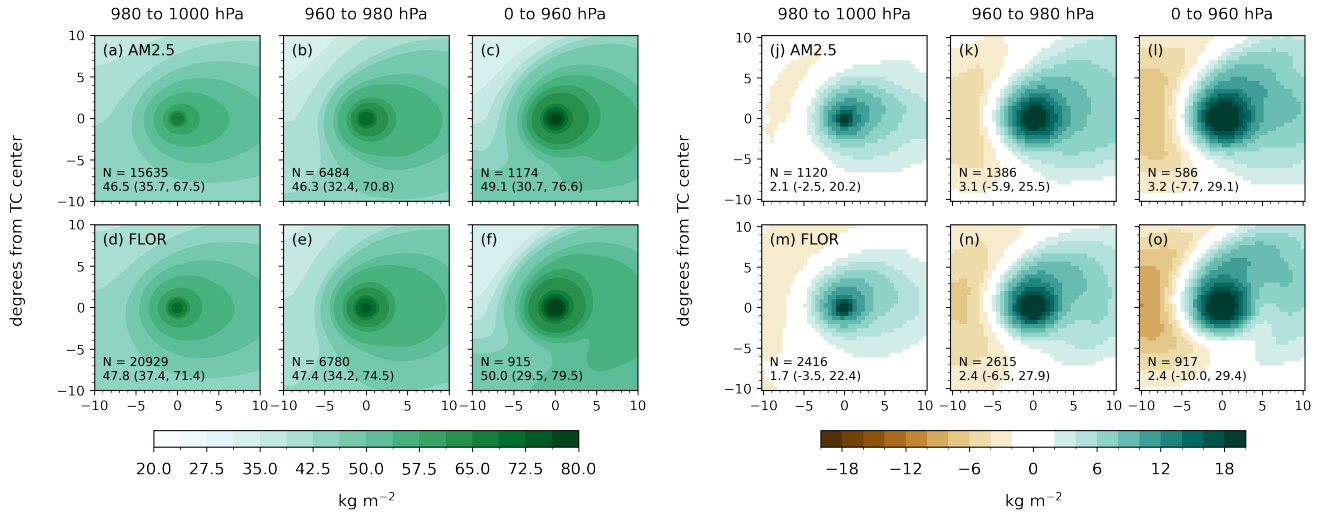


Fig. 6. As in Figure 2, for column-integrated water vapor composite means from AM2.5 and CM2.5-FOR.

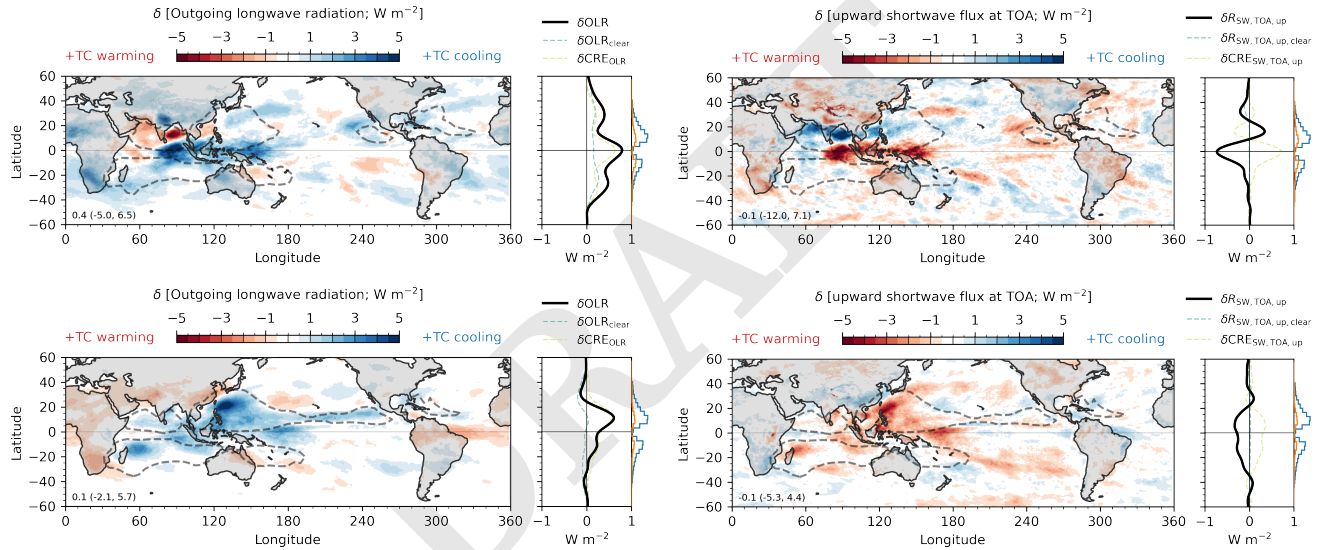


Fig. 7. As in Figure 3 for outgoing longwave radiation (OLR, panels a-c) and absorbed shortwave radiation (ASR, panels b-d) for AM2.5 (top row, panels a-b) and CM2.5-FOR (bottom row, panels c-d).

For any tropical cyclone (TC) snapshot quantity x_{TC} , first identify the corresponding day of year (1 to 366) when the snapshot was taken.

Using the determined day of year, extract the same quantity x for that specific day across all years in the multi-year dataset. This produces an array of values: $[x_{start}, \dots, x_n, \dots, x_{end}]$, where:

- x_{start} corresponds to the quantity in the dataset's first year
- x_{end} corresponds to the quantity in the dataset's final year - n represents intermediate years (start j n j end)

To ensure representative climatological sampling, values of x are chosen at each year within a 10-day window centered on the timestamp of x_{TC} . The climatological time mean \bar{x} is then computed by averaging all values in the array $[x_{start}, \dots, x_n, \dots, x_{end}]$.

The anomaly x'_{TC} is then computed by subtracting \bar{x} from the TC snapshot quantity x_{TC} : $x'_{TC} = x_{TC} - \bar{x}$.

ACKNOWLEDGMENTS. This material is based upon work supported by the U.S. Department of Energy, Office of Science, Office of Advanced Scientific Computing Research, Department of Energy Computational Science Graduate Fellowship (DOE CSGF) under award number DE-SC0024386. The authors would like to thank Jhordanne Jones, Levi Silvers, and Ming Zhao for helpful conversations that improved the quality of this manuscript.

1. JT Fasullo, KE Trenberth, The annual cycle of the energy budget, part ii: Meridional structures and poleward transports. *J. Clim.* **21**, 2313–2325 (2008).
2. RT Pierrehumbert, Thermostats, radiator fins, and the local runaway greenhouse. *J. atmospheric sciences* **52**, 1784–1806 (1995).

3. S Bony, et al., Thermodynamic control of anvil cloud amount. *Proc. Natl. Acad. Sci.* **113**, 8927–8932 (2016).
4. S Bony, et al., Observed modulation of the tropical radiation budget by deep convective organization and lower-tropospheric stability. *AGU advances* **1**, e2019AV000155 (2020).
5. IM Held, RS Hemler, V Ramaswamy, Radiative-convective equilibrium with explicit two-dimensional moist convection. *J. Atmospheric Sci.* **50**, 3909–3927 (1993).

993	6. TH Stein, CE Holloway, I Tobin, S Bony, Observed relationships between cloud vertical structure and convective aggregation over tropical ocean. <i>J. Clim.</i> 30 , 2187–2207 (2017).	1055
994	7. I Tobin, S Bony, R Roca, Observational evidence for relationships between the degree of aggregation of deep convection, water vapor, surface fluxes, and radiation. <i>J. Clim.</i> 25 , 6885–6904 (2012).	1056
995	8. AA Wing, et al., Clouds and convective self-aggregation in a multimodel ensemble of radiative-convective equilibrium simulations. <i>J. Adv. Model. Earth Syst.</i> 12 , e2020MS002138 (2020).	1057
996	9. T Becker, AA Wing, Understanding the extreme spread in climate sensitivity within the radiative-convective equilibrium model intercomparison project. <i>J. Adv. Model. Earth Syst.</i> 12 , e2020MS002165 (2020).	1058
997	10. D Coppin, S Bony, On the interplay between convective aggregation, surface temperature gradients, and climate sensitivity. <i>J. Adv. Model. Earth Syst.</i> 10 , 3123–3138 (2018).	1059
998	11. AG Pendergrass, Changing degree of convective organization as a mechanism for dynamic changes in extreme precipitation. <i>Curr. Clim. Chang. Reports</i> 6 , 47–54 (2020).	1060
999	12. M Khairoutdinov, K Emanuel, Rotating radiative-convective equilibrium simulated by a cloud-resolving model. <i>J. Adv. Model. Earth Syst.</i> 5 , 816–825 (2013).	1061
1000	13. C Muller, S Bony, What favors convective aggregation and why? <i>Geophys. Res. Lett.</i> 42 , 5626–5634 (2015).	1062
1001	14. CJ Muller, DM Romps, Acceleration of tropical cyclogenesis by self-aggregation feedbacks. <i>Proc. Natl. Acad. Sci.</i> 115 , 2930–2935 (2018).	1063
1002	15. AA Wing, SJ Camargo, AH Sobel, Role of radiative–convective feedbacks in spontaneous tropical cyclogenesis in idealized numerical simulations. <i>J. Atmospheric Sci.</i> 73 , 2633–2642 (2016).	1064
1003	16. SJ Camargo, AA Wing, Tropical cyclones in climate models. <i>Wiley Interdiscip. Rev. Clim. Chang.</i> 7 , 211–237 (2016).	1065
1004	17. T Knutson, et al., Tropical cyclones and climate change assessment: Part ii: Projected response to anthropogenic warming. <i>Bull. Am. Meteorol. Soc.</i> 101 , E303–E322 (2020).	1066
1005	18. KJ Walsh, et al., Tropical cyclones and climate change. <i>Wiley Interdiscip. Rev. Clim. Chang.</i> 7 , 65–89 (2016).	1067
1006	19. E Scoccimarro, et al., The typhoon-induced drying of the Maritime Continent. <i>Proc. Natl. Acad. Sci.</i> 117 , 3983–3988 (2020).	1068
1007	20. JH Ruppert Jr, AA Wing, X Tang, EL Duran, The critical role of cloud–infrared radiation feedback in tropical cyclone development. <i>Proc. Natl. Acad. Sci.</i> 117 , 27884–27892 (2020).	1069
1008	21. B Zhang, BJ Soden, GA Vecchi, W Yang, The role of radiative interactions in tropical cyclone development under realistic boundary conditions. <i>J. climate</i> 34 , 2079–2091 (2021).	1070
1009	22. Z Ma, J Fei, Y Lin, X Huang, Modulation of clouds and rainfall by tropical cyclone’s cold wakes. <i>Geophys. Res. Lett.</i> 47 , e2020GL088873 (2020).	1071
1010	23. W Mei, C Pasquero, Spatial and temporal characterization of sea surface temperature response to tropical cyclones. <i>J. Clim.</i> 26 , 3745–3765 (2013).	1072
1011	24. C Pasquero, F Desbiolles, AN Meroni, Air–sea interactions in the cold wakes of tropical cyclones. <i>Geophys. Res. Lett.</i> 48 , e2020GL091185 (2021).	1073
1012	25. J Zhang, Y Lin, Z Ma, Footprint of tropical cyclone cold wakes on top-of-atmosphere radiation. <i>Geophys. Res. Lett.</i> 48 , e2021GL094705 (2021).	1074
1013	26. JD Carstens, AA Wing, A spectrum of convective self-aggregation based on background rotation. <i>J. Adv. Model. Earth Syst.</i> 14 , e2021MS002860 (2022).	1075
1014	27. SN Wu, B Soden, D Nolan, Examining the role of cloud radiative interactions in tropical cyclone development using satellite measurements and wrf simulations. <i>Geophys. Res. Lett.</i> 48 , e2021GL093259 (2021).	1076
1015	28. L Hu, EA Ritchie, J Scott Tyo, Quantifying the cooling effect of tropical cyclone clouds on the climate system. <i>NPJ Clim. Atmospheric Sci.</i> 6 , 99 (2023).	1077
1016	29. RA Dare, JL McBride, Sea Surface Temperature Response to Tropical Cyclones. <i>Mon. Weather. Rev.</i> 139 , 3798–3808 (2011).	1078
1017	30. JF Price, Upper Ocean Response to a Hurricane. <i>J. Phys. Oceanogr.</i> 11 , 153–175 (1981).	1079
1018	31. M Zhao, Cloud Radiative Effects Associated With Daily Weather Regimes. <i>Geophys. Res. Lett.</i> 51 , e2024GL109090 (2024).	1080
1019	32. A Huang, H Li, RL Sriver, AV Fedorov, CM Brierley, Regional variations in the ocean response to tropical cyclones: Ocean mixing versus low cloud suppression. <i>Geophys. Res. Lett.</i> 44 , 1947–1955 (2017).	1081
1020	33. JD Carstens, AA Wing, Tropical Cyclogenesis From Self-Aggregated Convection in Numerical Simulations of Rotating Radiative-Convective Equilibrium. <i>J. Adv. Model. Earth Syst.</i> 12 , e2019MS002020 (2020).	1082
1021	34. C Muller, et al., Spontaneous Aggregation of Convective Storms. <i>Annu. Rev. Fluid Mech.</i> (2022).	1083
1022	35. AA Wing, et al., Clouds and Convective Self-Aggregation in a Multimodel Ensemble of Radiative-Convective Equilibrium Simulations. <i>J. Adv. Model. Earth Syst.</i> 12 , e2020MS002138 (2020).	1084
1023	36. GA Vecchi, et al., On the seasonal forecasting of regional tropical cyclone activity. <i>J. Clim.</i> 27 , 7994–8016 (2014).	1085
1024	37. TL Delworth, et al., Simulated climate and climate change in the gfdl cm2. 5 high-resolution coupled climate model. <i>J. Clim.</i> 25 , 2755–2781 (2012).	1086
1025	38. NA Rayner, et al., Global analyses of sea surface temperature, sea ice, and night marine air temperature since the late nineteenth century. <i>J. Geophys. Res. Atmospheres</i> 108 (2003).	1087
1026	39. NASA/LARC/SD/ASDC, Ceres and geo-enhanced toa, within-atmosphere and surface fluxes, clouds and aerosols 1-hourly terra-aqua edition4a (2017).	1088
1027	40. I Held, et al., Structure and performance of gfdl’s cm4. 0 climate model. <i>J. Adv. Model. Earth Syst.</i> 11 , 3691–3727 (2019).	1089
1028	41. G Rios, G Vecchi, W Yang, Reducing tropical cyclone activity in global climate models by evaporative suppression. <i>submitted to J. Geophys. Res. Atmospheres in review</i> (2025).	1090
1029		1091
1030		1092
1031		1093
1032		1094
1033		1095
1034		1096
1035		1097
1036		1098
1037		1099
1038		1100
1039		1101
1040		1102
1041		1103
1042		1104
1043		1105
1044		1106
1045		1107
1046		1108
1047		1109
1048		1110
1049		1111
1050		1112
1051		1113
1052		1114
1053		1115
1054		1116